

DRIFT: Driving Risk Inference via Field Transmission for Human-like Autonomous Driving

Zian Wang, Yiming Shu, Zejian Deng, Chen Sun *Member, IEEE*

Abstract—Risk fields offer spatially structured alternatives to scalar safety metrics. However, hand-crafted static risk field models struggle with occlusion and topology-driven propagation. We present DRIFT, a spatiotemporal risk field governed by an advection–diffusion–reaction partial differential equation (PDE), with an optional telegrapher term. DRIFT draws on three sources: anisotropic Gaussian kernels to capture velocity-induced risk, occlusion-aware latent hazards behind large vehicles, and topology-coupled merge-zone conflict pressure. We further introduce field-centric evaluation metrics to complement the existing Surrogate Safety Measures (SSMs), including Lane-Change Risk Differential, Temporal Anticipation Index, Occlusion Sensitivity Index, and Occlusion Response Latency. Experiments on real-world traffic datasets show that DRIFT reduces occlusion response latency by 52%, and lowers the near-collision rate under occlusion by 2.1% compared with selected baselines in synthetic scenarios. The code is available at <https://github.com/SAS-HKU/DRIFT.git>.

Index Terms—Spatiotemporal Risk Field Modeling, Field Transmission Dynamics, Occlusion-Aware Hazard Estimation, Human-like Autonomous Driving.

I. INTRODUCTION

Understanding and modeling risks in mixed traffic environments remain fundamental challenges for modern Intelligent Transportation Systems (ITS), especially in interactive scenarios such as highway merging and lane changing, where vehicles must reason about surrounding agents' intentions, constraints, and uncertainties [1], [2]. Traditional safety metrics provide useful signals, but they are typically pairwise, instantaneous, and scalar, making it difficult to capture the spatial structure of multi-agent interactions.

Field-based representations, also referred to as risk fields or potential fields, offer spatially structured alternatives by defining risk as a continuous scalar function over the Bird's Eye View (BEV) plane. Their local magnitudes and gradients encode hazard distribution and spatial influence, enabling downstream modules to reason beyond discrete agent locations [3]. Existing risk-field methods include hand-crafted

static potentials based on kinematics or interaction primitives [4], physics-informed dynamic fields with explicit transmission structure, and data-driven or hybrid risk maps that learn dense risk/occupancy representations from trajectory data [5]–[7]. However, occlusion and partial observability remain critical challenges, and existing evaluations still largely rely on surrogate safety measures or scenario stress tests [8].

Despite this progress, three limitations remain. First, many risk fields are static or frame-wise, and therefore lack a shared transmission law for temporal anticipation. Second, occlusion is often handled through masking or heuristic padding rather than explicit latent-risk propagation and clearance. Third, field models are commonly evaluated using scalar Surrogate Safety Measures (SSMs), such as Time-to-Collision (TTC), Post-Encroachment-Time (PET) [9], or downstream collision statistics [10], which cannot fully diagnose whether the spatial structure and propagation behavior of a risk field are correct, especially in occluded or far-ahead regions.

To address these gaps, we introduce **DRIFT: Driving Risk Inference via Field Transmission** governed by a partial differential equation (PDE)-based field transmission model, with structure depicted in Fig. 1. Our contributions are as follows:

- 1) A unified advection–diffusion–reaction PDE that provides a principled transmission substrate for risk, preserving temporal memory through decay, propagating hazards downstream through advection, and spreading spatial uncertainty through diffusion.
- 2) A geometry-coupled occlusion decay mechanism in which the field's local decay rate responds directly to the rate of change of the shadow mask.
- 3) A field-native evaluation protocol comprising behavioral, propagation, and occlusion-response metrics.

The remainder of this paper is structured as follows. Sections II and III formulate the problem and methodology. Section IV presents experiments, and Section V concludes the paper.

II. PRELIMINARIES

A. Modeling Risk Potential Field

We adopt a potential-field view in which risk is represented as a non-negative scalar potential over the BEV plane, where higher values indicate regions that should be avoided or treated conservatively by a downstream policy [11]. In

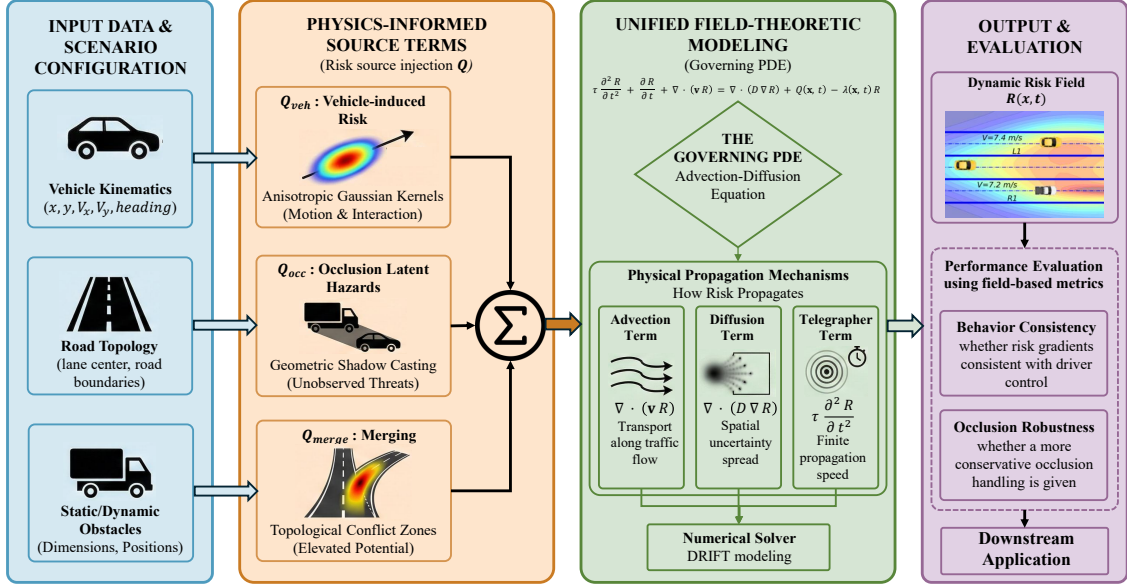


Fig. 1. Overall structure of the PDE-based risk inference via field transmission framework for human-like autonomous driving.

DRIFT, the field is defined in the ego-centric perception frame: $\Omega \subset \mathbb{R}^2$ denotes the spatial domain within the ego vehicle's sensor range, and $t \in [0, T]$. Formally, the risk field is denoted as: $R(\mathbf{x}, t) : \Omega \times [0, T] \rightarrow \mathbb{R}^+$, where $\mathbf{x} = (x, y) \in \mathbb{R}^2$ is a 2D spatial position vector in the BEV plane. At each time t , the scene contains the ego vehicle and surrounding agents indexed by i , each with state $(\mathbf{x}_i(t), \mathbf{v}_i(t), \mathbf{a}_i(t))$ expressed in the same BEV coordinates. Occlusion is modeled from the ego viewpoint via a time-varying shadow region $\Omega_{\text{occ}}(t)$ induced by large vehicles (e.g., truck-trailers), and a smoothed shadow mask $S(\mathbf{x}, t) \in [0, 1]$ for stable coupling to the field dynamics (Fig. 2).

B. Dataset Loading and Field Construction

We construct the time-indexed source term $Q(\mathbf{x}, t)$ and the corresponding field $R(\mathbf{x}, t)$ from raw trajectory logs. For BEV datasets, we parse the CSV tracks to obtain, for each frame, the ego and surrounding-agent states $(\mathbf{x}_i(t), \mathbf{v}_i(t), \mathbf{a}_i(t))$ in a common BEV coordinate system. These states are then converted into three additive sources: (i) a vehicle-interaction source Q_{veh} obtained by placing anisotropic Gaussian kernels at each agent; (ii) an occlusion source Q_{occ} obtained by computing the ego-view shadow mask $S(\mathbf{x}, t)$ and injecting latent hazard within the corresponding shadow region $\Omega_{\text{occ}}(t) \subset \Omega$; and (iii) a topology/merge source Q_{merge} derived from lane geometry and conflict-zone priors. The full source is $Q = Q_{\text{veh}} + Q_{\text{occ}} + Q_{\text{merge}}$, which is evaluated on a fixed BEV grid per frame and used to evolve the spatiotemporal field $R(\mathbf{x}, t)$ via the PDE transmission model described in Section III.

III. METHODOLOGY

A. Risk Field Transmission Model

Given the source field $Q(\mathbf{x}, t)$ constructed from the scene representation in Section II, DRIFT evolves the risk potential $R(\mathbf{x}, t)$ over the ego-centric BEV domain Ω using an advection–diffusion–reaction transmission model:

$$\frac{\partial R}{\partial t} = \underbrace{\nabla \cdot (D \nabla R)}_{\text{diffusion}} - \underbrace{\nabla \cdot (\mathbf{v} R)}_{\text{advection}} + \underbrace{Q(\mathbf{x}, t)}_{\text{source}} - \underbrace{\lambda(\mathbf{x}, t) R}_{\text{decay}}. \quad (1)$$

Here, $\mathbf{v}(\mathbf{x}, t) = \mathbf{v}_{\text{flow}} + \mathbf{v}_{\text{topo}}$ is the effective transmission velocity, $D(\mathbf{x}, t)$ is the spatial diffusivity, and $\lambda(\mathbf{x}, t)$ is the decay rate. An optional inertial telegrapher term $\tau \partial^2 R / \partial t^2$ can be added to the left-hand side to enforce finite propagation speed; in our experiments, we set $\tau = 0$ for computational efficiency and numerical stability.

The total source field is the additive composition:

$$Q(\mathbf{x}, t) = Q_{\text{veh}}(\mathbf{x}, t) + Q_{\text{occ}}(\mathbf{x}, t) + Q_{\text{merge}}(\mathbf{x}, t), \quad (2)$$

where:

$$Q_{\text{veh}}(\mathbf{x}, t) = \sum_i w_i G(\mathbf{x}; \boldsymbol{\mu}_i, \mathbf{P}_i), \quad (3)$$

$$Q_{\text{occ}}(\mathbf{x}, t) = \mathbf{1}_{\Omega_{\text{occ}}(t)}(\mathbf{x}) g(\mathbf{x}, t) p_{\text{emerge}}(\mathbf{x}, t), \quad (4)$$

$$Q_{\text{merge}}(\mathbf{x}, t) = k_{\text{amb}} \rho_{\text{merge}}(\mathbf{x}) + k_{\text{veh}} \rho_{\text{merge}}(\mathbf{x}) \rho_{\text{veh}}(\mathbf{x}, t). \quad (5)$$

The vehicle term places anisotropic Gaussian kernels at observed agents, the occlusion term injects latent risk inside the ego-view shadow region, and the merge term encodes topology-driven conflict pressure near merge zones. These sources anchor the field to scene evidence, while the shared operator in (1) propagates, smooths, and clears risk over time.

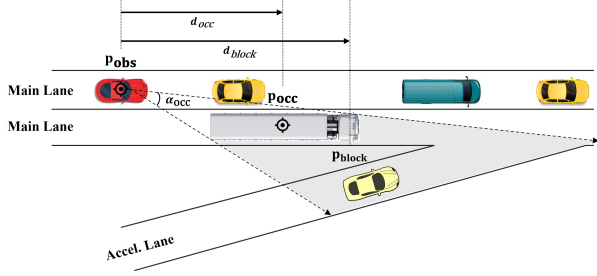


Fig. 2. Occlusion geometry in highway merging. The ego vehicle (observer) in the Main Lane with the position \mathbf{p}_{obs} in the main lane cannot perceive the blocked vehicle with position $\mathbf{p}_{\text{block}}$ in the Acceleration (Accel.) Lane due to the heavy truck (occluder) with the position \mathbf{p}_{occ} .

B. Model Design Rationale

Role of each PDE term. The four components are complementary rather than interchangeable. The source term $Q(\mathbf{x}, t)$ anchors the field to observable scene evidence (vehicle interaction, occlusion, and topology conflict). Advection transmits injected hazards along the effective flow, allowing risk to emerge before an interaction reaches the ego vehicle. Diffusion smooths sharp peaks and spreads positional uncertainty, which is especially important inside occlusion regions where the hidden-agent distribution is broad. Decay removes stale hazard and prevents persistent wakes from dominating the map after the causal interaction has ended or visibility has returned.

Initialization and boundary conditions. We initialize the field as $R(\mathbf{x}, 0) = 0$ so that risk is purely evidence-driven and does not inherit arbitrary priors. At the sensor boundary $\partial\Omega$, we apply zero-flux Neumann conditions $\partial R / \partial n|_{\partial\Omega} = 0$ to avoid numerical loss of hazard through the boundary of the perceived domain. Downstream, an absorbing sponge layer ($\lambda_{\text{sponge}} \propto \|\mathbf{x} - \mathbf{x}_s\|^2$) dissipates advected risk as it exits the sensor range, preventing artificial back-reflections that would otherwise re-contaminate upstream estimates.

Occlusion Handling. The decay rate is coupled to the shadow mask $S(\mathbf{x}, t)$. When a shadow expands, decay is reduced so that latent risk can accumulate; when a shadow retreats, decay is increased to clear risk no longer supported by occlusion. We initialize $R(\mathbf{x}, 0) = 0$, use zero-flux boundary conditions at the sensor boundary, and apply a downstream sponge layer to dissipate risk leaving the observable domain.

C. Occlusion-Aware Scenario Extraction

To evaluate occlusion handling under a consistent protocol, we first extract occlusion windows from the raw trajectory logs and then apply all methods to the same selected intervals. Algorithm 1 details the occlusion-window extraction process and relevant parameters. Let k denote the frame index, $t_k = k/\nu$ the corresponding time, and $\mathbf{p}_j^k \in \mathbb{R}^2$ the BEV position of agent j at frame k . For the ego vehicle e , we transform each candidate heavy vehicle j into the ego body frame as:

$$\mathbf{r}_{e,j}^k = \mathbf{R}(\psi_e^k) (\mathbf{p}_j^k - \mathbf{p}_e^k), \quad \mathbf{R}(\psi_e^k) = \begin{bmatrix} \cos \psi_e^k & \sin \psi_e^k \\ -\sin \psi_e^k & \cos \psi_e^k \end{bmatrix}, \quad (6)$$

Algorithm 1 Occlusion-window extraction

Require: Recording $\mathcal{D} = \{(\mathbf{p}_j^k, \psi_j^k, c_j)\}_{j,k}$, ego id e , frame rate ν , padding time T_{pad} , heavy-class set $\mathcal{C}_{\text{heavy}}$

Ensure: Occlusion-window set \mathcal{W}_{occ}

- 1: $\mathcal{F}_{\text{occ}} \leftarrow \emptyset$
- 2: $\mathcal{Z}_{\text{front}} \leftarrow \{(r_{\parallel}, r_{\perp}) : 0 < r_{\parallel} < L_{\parallel}, |r_{\perp}| < L_{\perp}\}$
- 3: **for all** frames $k = 1, \dots, K$ in which ego e is active **do**
- 4: Obtain ego pose $(\mathbf{p}_e^k, \psi_e^k)$
- 5: $\mathbf{R}_e^k \leftarrow \begin{bmatrix} \cos \psi_e^k & \sin \psi_e^k \\ -\sin \psi_e^k & \cos \psi_e^k \end{bmatrix}$
- 6: **for all** agents $j \neq e$ active at frame k with $c_j \in \mathcal{C}_{\text{heavy}}$ **do**
- 7: $\mathbf{r}_{e,j}^k \leftarrow \mathbf{R}_e^k (\mathbf{p}_j^k - \mathbf{p}_e^k)$
- 8: **if** $\mathbf{r}_{e,j}^k \in \mathcal{Z}_{\text{front}}$ **then**
- 9: $\mathcal{F}_{\text{occ}} \leftarrow \mathcal{F}_{\text{occ}} \cup \{k\}$
- 10: **break**
- 11: **end if**
- 12: **end for**
- 13: **end for**
- 14: Group \mathcal{F}_{occ} into maximal contiguous runs $\{[s_w, e_w]\}_{w=1}^W$
- 15: $\Delta_{\text{pad}} \leftarrow \lceil T_{\text{pad}} \nu \rceil$
- 16: **return** $\mathcal{W}_{\text{occ}} = \{[\max(1, s_w - \Delta_{\text{pad}}), \min(K, e_w + \Delta_{\text{pad}})]\}_{w=1}^W$

where $\mathbf{r}_{e,j}^k = (r_{\parallel,e,j}^k, r_{\perp,e,j}^k)^{\top}$ contains the longitudinal and lateral relative coordinates in the ego frame. A frame is flagged as occlusion-relevant if at least one heavy-class agent lies in the forward selection zone:

$$\mathcal{Z}_{\text{front}} = \{\mathbf{r} = (r_{\parallel}, r_{\perp}) : 0 < r_{\parallel} < 90 \text{ m}, |r_{\perp}| < 18 \text{ m}\}. \quad (7)$$

The set of flagged frames is therefore:

$$\mathcal{F}_{\text{occ}} = \{k : \exists j \neq e, c_j \in \mathcal{C}_{\text{heavy}}, \mathbf{r}_{e,j}^k \in \mathcal{Z}_{\text{front}}\}. \quad (8)$$

We group \mathcal{F}_{occ} into maximal contiguous runs and pad each run by $T_{\text{pad}} = 2 \text{ s}$ on both sides.

Connection to the PDE field variables. The extraction procedure does not redefine the occlusion field $\Omega_{\text{occ}}(t)$ used in (4). Instead, it selects the temporal intervals in which such occlusion-aware field modeling is evaluated. Specifically, a forward heavy-vehicle selection zone $\mathcal{Z}_{\text{front}}$ is used to identify occlusion-relevant frames from raw trajectories. For each selected frame t_k , the ego-view shadow mask $S(\mathbf{x}, t_k)$ and the corresponding shadow region $\Omega_{\text{occ}}(t_k) = \{\mathbf{x} \in \Omega : S(\mathbf{x}, t_k) > \theta_S\}$ are then computed on the same BEV grid as the risk field.

For every $k \in \mathcal{W}_{\text{occ}}$, we compute $S(\mathbf{x}, t_k)$, $\Omega_{\text{occ}}(t_k)$, $Q_{\text{occ}}(\mathbf{x}, t_k)$, and $\lambda(\mathbf{x}, t_k)$ on the same BEV grid used by (1). Here, $L_{\parallel} = 90 \text{ m}$ and $L_{\perp} = 18 \text{ m}$ define the ego-frame selection zone $\mathcal{Z}_{\text{front}}$ for extracting evaluation windows. $T_{\text{pad}} = 2 \text{ s}$ preserves pre- and post-occlusion field evolution, and $\mathcal{C}_{\text{heavy}}$ denotes truck/trailer occluder classes.

D. Metrics and Evaluation Framework

Limitations of Traditional SSMs for Field Evaluation
Traditional SSMs are insufficient for evaluating continuous

risk fields because they reduce safety to pairwise, instantaneous scalars and discard spatial gradients, directional structure, and field coherence across the BEV domain. They are also visibility-blind: TTC and related measures are undefined for occluded agents, so they cannot distinguish conservative shadow risk from risk collapse. Finally, they are reactive under constant-velocity assumptions and therefore miss the lead-time benefit introduced by advection-based propagation. We therefore introduce field-native metrics grounded in observable trajectory data and independent of the field model being assessed:

LCRD (Lane-Change Risk Differential) is the fraction of recorded lane changes that move toward a lower-risk cell:

$$\text{LCRD} = \frac{|\{i: R(\mathbf{x}_{\text{curr},i}) > R(\mathbf{x}_{\text{target},i})\}|}{|\text{all lane changes}|}. \quad (9)$$

TAI (Temporal Anticipation Index) measures how early the field threshold is crossed relative to the hazardous event, normalized by human reaction time $t_r = 1.5$ s:

$$\text{TAI} = \frac{1}{N} \sum_i \frac{t_{\text{event}}^i - t_{\text{field}}^i}{t_r}. \quad (10)$$

RPR (Risk Persistence Ratio) quantifies post-event risk memory over a $\Delta T = 2$ s window:

$$\text{RPR} = \frac{\int_{t_e}^{t_e + \Delta T} R(\mathbf{x}, t) dt}{R_{\text{peak}} \cdot \Delta T}. \quad (11)$$

OSI, **ORL**, **$\Delta\text{Coll.}\%$** , and **Temp.** characterize occlusion robustness. $\text{OSI} = \Delta \bar{R} / \Delta \rho$ measures risk sensitivity to the occlusion ratio ρ ; $\text{ORL} = |t_{R>\theta} - t_{\text{shadow}}|$ measures shadow response latency; $\Delta\text{Coll.}$ counts the relative increase in near-collision events under occlusion versus full visibility; and **Temp.** is the frame-to-frame autocorrelation of region-mean risk.

IV. EXPERIMENTS AND RESULTS

A. Experimental Setup

We evaluate on exiD [12], rounD [13], and inD [14] on a unified 150×70 BEV grid at 20 Hz. Baselines include static physics-informed fields (TPF [4], APF [11], DPDRF [15]) and dynamic data-driven fields (EDRF [5], RiskNet [7]). Selected PDE and source parameters are listed in Table I.

B. Behavior Consistency

We first evaluate behavior consistency, which measures whether field structure agrees with recorded driver decisions. We report LCRD and RPR for all methods, since both are defined for static and dynamic fields. Table II summarizes all results. DRIFT achieves the best overall alignment with observed driver actions. It attains an LCRD of 89% versus 82% (RiskNet) and 78% (EDRF), indicating that recorded lane changes are more often directed toward lower-risk regions. DRIFT also yields the highest post-event risk retention (RPR 0.74), suggesting that it preserves salient interaction risk without excessive lingering.

TABLE I
SELECTED PDE AND SOURCE PARAMETERS.

| Symbol | Value | Unit | Description |
|----------------------------------|-----------|-------------------|---|
| <i>Source Parameters</i> | | | |
| σ_x, σ_y | 12.0, 3.0 | m | Longitudinal/lateral kernel spread |
| L_{prox} | 50.0 | m | Distance attenuation length |
| v_{ref} | 5.0 | m/s | Relative-speed reference |
| $\beta_a, \beta_{\text{brake}}$ | 0.3, 0.8 | — | Acceleration/braking source weights |
| a_{ref} | 3.0 | m/s ² | Acceleration normalization |
| $\gamma_a, t_{\text{react}}$ | 0.5, 1.5 | —, s | Braking kernel shift |
| <i>PDE Parameters</i> | | | |
| D_0, D_{occ} | 1.0, 3.0 | m ² /s | Base and occlusion diffusion |
| $\lambda_0, \lambda_{\text{sh}}$ | 0.15, 1.3 | 1/s | Base and shadow decay |
| λ_g | 1.0 | 1/s | Geometry-coupled decay coefficient |
| <i>Merge Parameters</i> | | | |
| $k_{\text{amb}}, k_{\text{veh}}$ | 0.08, 0.6 | — | Ambient and vehicle-gated merge weights |

C. Propagation Advantage

Since static fields are recomputed frame-by-frame and carry no temporal memory, TAI and ORL are structurally undefined for static baselines; we therefore report these metrics only for dynamic methods. DRIFT provides the largest anticipatory margin. It reaches $\text{TAI} = 0.41$ (corresponding to ≈ 0.62 s at $t_r = 1.5$ s), compared with 0.24 for RiskNet and 0.18 for EDRF. This improvement reflects PDE-driven transmission that carries injected hazard downstream as a structured wake, rather than reacting only at the onset of conflict.

D. Occlusion Robustness

Occlusion-robustness metrics evaluate whether the field remains conservative inside shadows while clearing latent risk promptly once visibility returns. We report OSI, ORL, $\Delta\text{Coll.}$, and **Temp.** to cover sensitivity, response latency, safety impact, and temporal stability.

DRIFT produces the most conservative yet responsive field evolution under occlusion. It achieves the highest occlusion sensitivity (OSI 0.52) and the fastest occlusion response (ORL 0.31 s), while reducing the near-collision rate increase under occlusion to +1.4% (vs. +3.5% for RiskNet and +4.7% for EDRF). DRIFT also attains the strongest temporal stability (**Temp.** 0.91), consistent with rapid clearance of latent risk once visibility is restored via geometry-coupled decay.

Note on static baselines. TAI and ORL are shown as “—” for static methods, namely TPF, APF, and DPDRF, because these metrics are structurally undefined for frame-wise fields with no temporal memory. Fig. 3 qualitatively compares DRIFT with TPF and APF on rounD roundabout, inD intersection, and exiD highway-ramp scenarios. The static baselines tend to assign broad and nearly uniform risk around visible objects or road geometry, which can activate redundant regions that are not directly involved in the current vehicle interaction. In contrast, DRIFT treats risk as propagated information: heavy

TABLE II
PERFORMANCE COMPARISON ACROSS ALL METRICS. “-” DENOTES METRICS THAT ARE STRUCTURALLY UNDEFINED FOR NON-TEMPORAL (STATIC) FORMULATIONS.

| Method | Behavior Consistency | | Propagation Advantage | | Occlusion Robustness | | | |
|----------------------------------|----------------------|----------------|-----------------------|---------------------|----------------------|------------------|-----------------------------|------------------|
| | LCRD \uparrow | RPR \uparrow | TAI \uparrow | (TAI $\times t_r$) | OSI \uparrow | ORL \downarrow | Δ Coll. \downarrow | Temp. \uparrow |
| <i>Physics-Informed (Static)</i> | | | | | | | | |
| TPF [4] | 62% | 0.38 | - \dagger | | 0.08 | - | +9.3% | 0.61 |
| GVF [16] | 71% | 0.42 | - \dagger | | 0.12 | - | +8.1% | 0.72 |
| DPDRF [15] | 68% | 0.41 | - \dagger | | 0.15 | - | +6.8% | 0.68 |
| <i>Dynamic (Data-Driven)</i> | | | | | | | | |
| EDRF [5] | 78% | 0.61 | 0.18 | (+0.27 s) | 0.28 | 0.82 s | +4.7% | 0.81 |
| RiskNet [7] | 82% | 0.67 | 0.24 | (+0.36 s) | 0.35 | 0.65 s | +3.5% | 0.85 |
| DRIFT (Ours) | 89% | 0.74 | 0.41 | (+0.62 s) | 0.52 | 0.31 s | +1.4% | 0.91 |

\dagger TAI and ORL are undefined for static (frame-wise) risk fields because these methods recompute risk from instantaneous states and carry no temporal memory. Reporting TAI ≈ 0 for static methods would be misleading, as it conflates a structural impossibility with a measurable outcome.

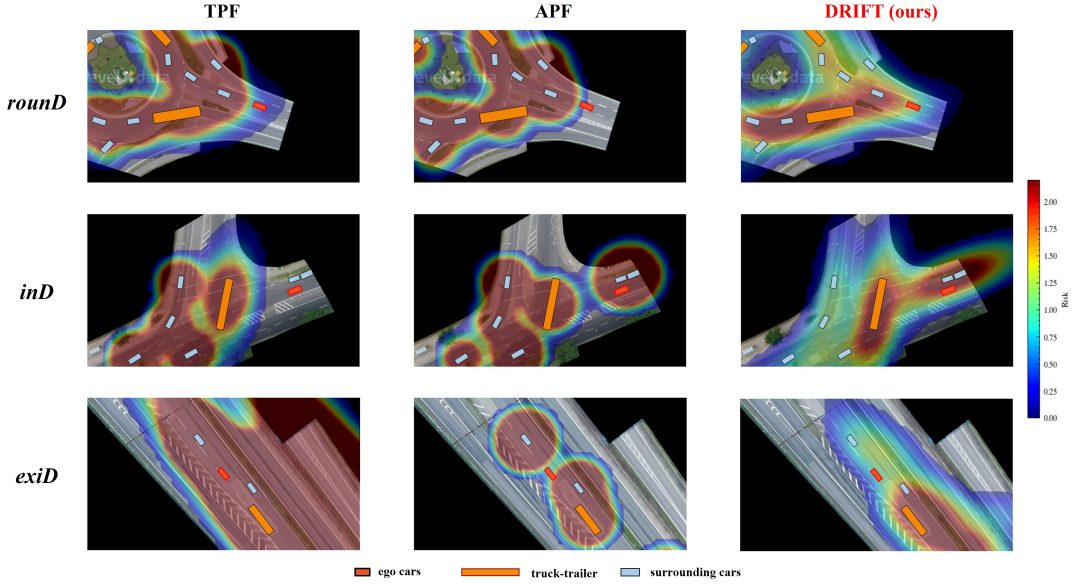


Fig. 3. Risk field modeling on historical ego trajectories recorded in various traffic scenarios.

truck-trailer occlusions induce latent risk that is transmitted along plausible traffic-flow and conflict directions rather than being spread as a static potential.

E. Ablation Study

In Table III, we ablate individual PDE terms. Adding advection raises TAI from 0.12 to 0.35 (+0.23), confirming that downstream transmission drives temporal anticipation. Diffusion improves occlusion conservatism (OSI 0.35 \rightarrow 0.42) by spreading latent hazard energy beyond the geometric shadow boundary. Geometry-coupled decay (full model) is the primary driver of fast visibility response (ORL 0.62 \rightarrow 0.31 s) and temporal consistency (0.85 \rightarrow 0.91).

The risk field visualizations in Fig. 4 complements Table III by visualizing the spatial effect of each PDE term on the same scenario snapshot. With source terms alone (upper left), risk is sharply localized around each vehicle and conflict zone with no spatial spread. Adding diffusion (upper right) produces smooth halos that extend uncertainty

TABLE III
ABLATION: PDE TERM CONTRIBUTIONS

| Config. | TAI \uparrow | RPR \uparrow | OSI \uparrow | ORL \downarrow | Temp. \uparrow |
|----------------|----------------|----------------|----------------|------------------|------------------|
| Source only | 0.08 | 0.51 | 0.35 | 0.95 s | 0.65 |
| + Diffusion | 0.12 | 0.58 | 0.42 | 0.78 s | 0.72 |
| + Advection | 0.35 | 0.66 | 0.44 | 0.62 s | 0.85 |
| + Decay (full) | 0.41 | 0.74 | 0.52 | 0.31 s | 0.91 |

into adjacent cells, raising OSI but introducing no directional structure. Adding advection without decay (lower left) creates a clear downstream “wake” pattern in which risk trails behind interacting vehicles along the traffic flow direction, explaining the large TAI jump (0.12 \rightarrow 0.35) but also producing residual risk that lingers after agents depart. The full model with geometry-coupled decay (lower right) retains the directional wake while actively clearing stale hazard, yielding the highest temporal consistency (0.91) and the fastest occlusion response (ORL 0.31 s).

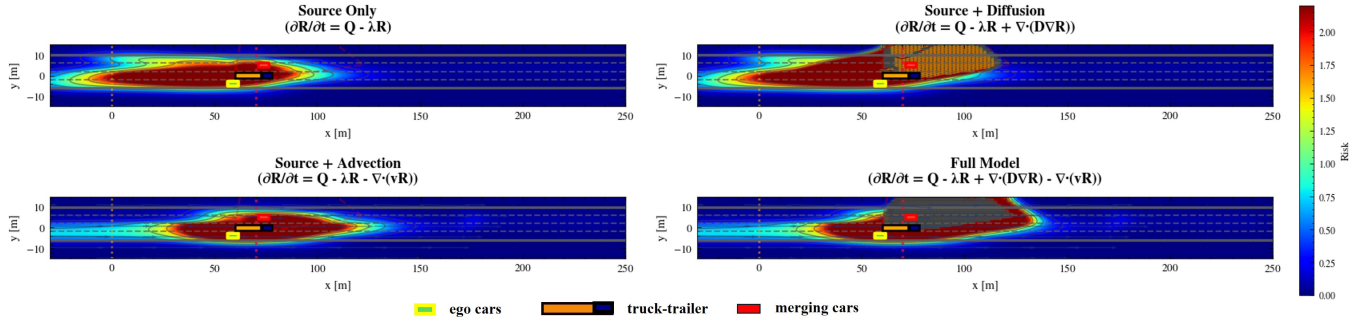


Fig. 4. Risk field snapshots for four ablation settings on the same highway merge scene: source-only, +diffusion, +advection, and full DRIFT (+geometry-coupled decay).

V. CONCLUSION

We presented DRIFT, a physics-informed spatiotemporal field modeling framework that explicitly propagates risk governed by a PDE transmission model. This formulation yields interpretable spatial risk structure and stable temporal dynamics, while enabling fast risk clearance when visibility is restored through geometry-coupled decay. The parameters of the PDE formulation remain tunable. Experiments on occlusion/merge scenarios from BEV datasets show that DRIFT better aligns field gradients with recorded driver actions and provides earlier warning compared to static fields and learned risk maps in the literature, while remaining robust under severe occlusion. Future work will extend DRIFT to a universal risk modeling that handles richer intersection geometries, more complex traffic scenarios, and multi-agent motion planning, and to integrate learned components such as uncertainty-aware sources and map priors.

ACKNOWLEDGMENT

The authors would like to acknowledge the financial support provided by the University Grants Committee of Hong Kong through the Early Career Scheme (Grant No. GRF/ECS-27206525).

REFERENCES

- [1] Z. Cheng, J. Zhu, Z. Feng, M. Yang, W. Zhang, and J. Chen, "Driving safety risk analysis and assessment in a mixed driving environment of connected and non-connected vehicles: a systematic survey," *IEEE Transactions on Intelligent Transportation Systems*, 2025.
- [2] C. Sun, R. Zhang, Y. Lu, Y. Cui, Z. Deng, D. Cao, and A. Khajepour, "Toward ensuring safety for autonomous driving perception: Standardization progress, research advances, and perspectives," *IEEE Transactions on Intelligent Transportation Systems*, vol. 25, no. 5, pp. 3286–3304, 2023.
- [3] V. Rasidescu and H. Taghavifar, "Artificial potential fields-enhanced socially intelligent path-planning for autonomous vehicles using type 2 fuzzy systems," in *2024 IEEE 27th International Conference on Intelligent Transportation Systems (ITSC)*. IEEE, 2024, pp. 2599–2605.
- [4] Y. Wang, N. Lyu, and J. Wen, "Modeling risk potential fields for mandatory lane changes in intelligent connected vehicle environment," *Expert Systems with Applications*, vol. 255, p. 124814, 2024.
- [5] J. Jiang, Z. Han, Y. Wang, M. Cai, Q. Meng, Q. Xu, and J. Wang, "Edrf: Enhanced driving risk field based on multimodal trajectory prediction and its applications," in *2024 IEEE 27th International Conference on Intelligent Transportation Systems (ITSC)*. IEEE, 2024, pp. 2287–2293.
- [6] Z. Wang, B. Shi, J. Zhang, X. Zhu, J. Zhou, B. Xu, and B. Li, "A data-driven spatio-temporal driving risk field mechanism for path planning," *Expert Systems with Applications*, p. 129834, 2025.
- [7] Q. Liu, H. Huang, S. Zhao, L. Shi, S. Ahn, and X. Li, "Risknet: interaction-aware risk forecasting for autonomous driving in long-tail scenarios," *Transportation Research Part E: Logistics and Transportation Review*, vol. 205, p. 104478, 2026.
- [8] Y. Tian, H. Pei, Y. Shi, Y. Zhang, D. Yao, L. Xiao, and B. Chen, "Driving risk field model and its application in trajectory planning: A new perspective," *IEEE Transactions on Intelligent Transportation Systems*, 2025.
- [9] X. Hou, M. Gan, W. Wu, Y. Ji, S. Zhao, and J. Chen, "Equipping with cognition: interactive motion planning using metacognitive-attribution inspired reinforcement learning for autonomous vehicles," *IEEE Transactions on Intelligent Transportation Systems*, 2024.
- [10] Z. Ma, H. Zhang, C. Hong, S. Xu, D. Zhang, J. Zhou, Z. Chen, and B. Li, "Modeling of driving risk fields considering vehicle-lane interactions and its application in car-following model," *Physica A: Statistical Mechanics and its Applications*, p. 131086, 2025.
- [11] S. Xie, J. Hu, P. Bhowmick, Z. Ding, and F. Arvin, "Distributed motion planning for safe autonomous vehicle overtaking via artificial potential field," *IEEE Transactions on Intelligent Transportation Systems*, vol. 23, no. 11, pp. 21 531–21 547, 2022.
- [12] T. Moers, L. Vater, R. Krajewski, J. Bock, A. Zlocki, and L. Eckstein, "The exid dataset: A real-world trajectory dataset of highly interactive highway scenarios in germany," in *2022 IEEE Intelligent Vehicles Symposium (IV)*. IEEE, 2022, pp. 958–964.
- [13] R. Krajewski, T. Moers, J. Bock, L. Vater, and L. Eckstein, "The round dataset: A drone dataset of road user trajectories at roundabouts in germany," in *2020 IEEE 23rd International Conference on Intelligent Transportation Systems (ITSC)*. IEEE, 2020, pp. 1–6.
- [14] J. Bock, R. Krajewski, T. Moers, S. Runde, L. Vater, and L. Eckstein, "The ind dataset: A drone dataset of naturalistic road user trajectories at german intersections," in *2020 IEEE Intelligent Vehicles Symposium (IV)*. IEEE, 2020, pp. 1929–1934.
- [15] J. Liu, X. Sheng, L. Tan, W. Zhang, P. Zhang, and K. Liu, "Dpdrf: Dynamic predictive driving risk field based on multi-agent trajectory prediction and digital twins system," *IEEE Transactions on Vehicular Technology*, 2025.
- [16] C. Zhang, J. Zhu, W. Wang, and J. Xi, "Spatiotemporal learning of multivehicle interaction patterns in lane-change scenarios," *IEEE Transactions on Intelligent Transportation Systems*, vol. 23, no. 7, pp. 6446–6459, 2021.